analytical chemistry

pubs.acs.org/ac Article

Two-phase Porous Media Flow Model Based on the Incompressible Navier–Stokes Equation

Hui Ma, Tamara L. Kinzer-Ursem,* and Jacqueline C. Linnes*

Cite This: *Anal. Chem.* 2024, 96, 5265–5273 Read Online

ACCESS | Metrics & More | Article Recommendations | Supporting Information

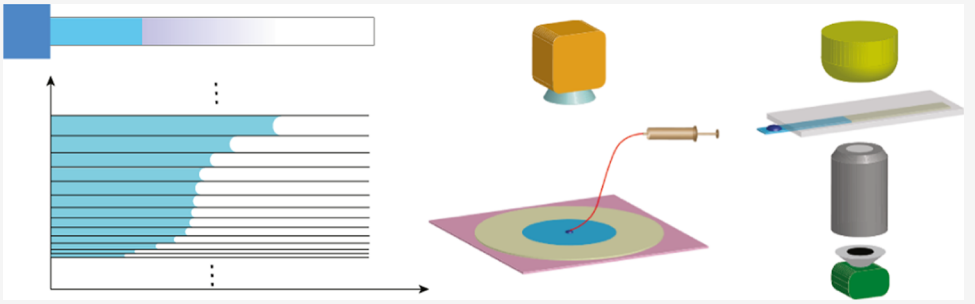

ABSTRACT: Two-phase porous media flow is important in many applications from drug delivery to groundwater diffusion and oil recovery and is of particular interest to biomedical diagnostic test developers using cellulose and nitrocellulose membranes with limited fluid sample volumes. This work presents a new two-phase porous media flow model based on the incompressible Navier–Stokes equation. The model aims to address the limitations of existing methods by incorporating a partial saturation distribution in porous media to account for limited fluid volumes. The basic parameters of the model are the pore size distribution and the contact angle. To validate the model, we solved five analytical solutions and compared them to corresponding experimental data. The experimentally measured penetration length data agreed with the model predictions, demonstrating model accuracy. Our findings suggest that this new two-phase porous media flow model can provide a valuable tool for researchers developing fluidic assays in paper and other porous media.

INTRODUCTION

Porous media comprise a wide range of materials, including natural substances such as soil, wood, and rock, as well as man-made materials like foamed metal, paper, and ceramics. The flow of fluids through these porous materials is driven either by capillary pressure or external pressure.[1−3] While porous media exhibit a discrete nature on the microscale, they are generally considered continuous on the macro-scale.[4] This statistical stability makes fluid flow in porous media an intriguing research subject. The single-phase flow in porous media does not have capillary pressure due to the absence of a solid/fluid/fluid interface. In such cases, Darcy's law, summarized from experimental data on water flow through sand, provides an effective description of the flow.[5−8] To account for the viscosity effects, the Brinkman equation was derived and modified based on Darcy's law, which remains applicable to single-phase flow scenarios.[9−11]

In the context of a multiphase flow, capillary pressure plays a crucial role, particularly in the case of immiscible two-phase systems such as water/air and water/oil. The Lucas–Washburn equation, originally developed to describe fluid flow in cylindrical tubing, finds utility in characterizing liquid flow within porous media.[12−15] However, the one-dimensional nature of the Lucas–Washburn equation limits its application to higher-dimensional practical scenarios. Furthermore, water–air two-phase flow often exhibits a partially saturated region between fully saturated and dry areas. While the Lucas–Washburn equation determines the location of the water–air interface, it cannot provide information about water content. In contrast, by defining a capillary potential numerically equivalent to capillary pressure, the Richards equation establishes a way to indicate the distribution of partial saturation in porous media flows.[16−19] This assumption of the equivalent capillary pressure and potential is typically satisfied due to the low Reynolds number of porous media flow. The Richards equation also incorporates the assumption that permeability and capillary potential are functions of the water content, resulting in a solution that accounts for both saturation and partial saturation distribution. The Richards equation was initially developed for soil physics and has found application in various fields such as hydrology, geology, and

Received: December 31, 2023
Revised: March 4, 2024
Accepted: March 5, 2024
Published: March 19, 2024

https://doi.org/10.1021/acs.analchem.3c05982
Anal. Chem. 2024, 96, 5265–5273

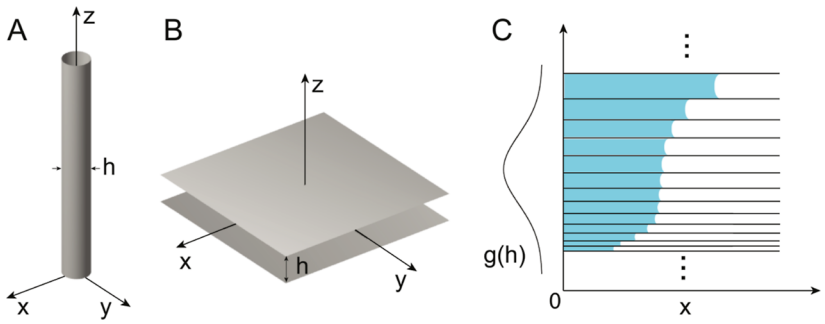

Figure 1. Model components (A) geometry of tubing, with no-slip boundary condition on the cylindrical wall. (B) A flow layer, the basic unit of our model. Fluids flow between the two surfaces. (C) Side view of the flow layer set with heights obeying Gaussian distribution. Water/air flows with different velocities in the various layers.

paper-based point-of-care testing (POCT) involving cellulose and nitrocellulose membranes as porous media.[20−26] However, the Richards equation assumes that pressure is a function of water content, which applies at the macroscale. The model presented here seeks to elucidate flow effects on the microscale. Understanding the flow of biomedical sample solutions through these membranes is critical for the design of improved POCT devices, particularly, as biomedical samples often have limited volumes. While several numerical models have been proposed to account for microlevel structures within porous media, their computational intensity and dependence on detailed pore distribution information limit their practicality.[27−29]

We present a novel two-phase porous media flow model based on the incompressible Navier−Stokes equation and the phase-field method incorporating saturation and partial saturation distribution, which we call the flow layer set model. The fundamental configuration of the model consists of two parallel plates with fluid flows between them. The velocity field is transformed into the Poiseuille flow in 2D and 3D domains. By incorporating parameters such as the contact angle, water/air surface tension, mean pore size, and standard deviation, our model enables the calculation of the saturation and partial saturation distribution. We validated the model by solving five analytical problems including 1D, 2D circular, 2D fan-strip, 3D spherical, and the permeability expression of Darcy's law. The models are helpful for the study of lateral flow assays, radially multiplexed detection assays, controlled flow rate pumps, and 3D paper networks.[30−38] To assess the flow layer set model's accuracy, we implemented experiments on nitrocellulose membranes in both 1D and 2D scenarios. The experimental data exhibited excellent agreement with the analytical solutions, highlighting its superior performance and potential applications, including paper-based microfluidics, lateral flow assays, paper chromatography, etc.

METHODS

Model Building. Capillary tubing is a suitable model for studying porous media due to its similarity to pores at the microlevel, with a no-slip boundary condition prevailing around the fluids, except at the inlet and outlet (Figure 1A). As a result, the Lucas−Washburn equation can effectively indicate the water−air interface within porous media. By solving the Poiseuille flow in capillary tubing derived from the Navier−Stokes equation, valuable insights can be gained.

$$\frac{1}{r}\frac{\partial}{\partial r}\left(r\frac{\partial v_z}{\partial r}\right) = \frac{1}{\mu}\frac{\partial p}{\partial z} \tag{1}$$

$$v_z\left(\frac{h}{2}\right) = 0 \tag{2}$$

$$v_z = \frac{h^2}{4\mu}\frac{\partial p}{\partial z}\left[\left(\frac{r}{h}\right)^2 - \frac{1}{4}\right] \tag{3}$$

where r and z are the components of the cylindrical coordinate system, v_z is the z component of the velocity field, μ is the dynamic viscosity, p is the pressure, and h is the diameter of the tubing. The momentum equation represented by eqs 1 and 2 is the no-slip boundary condition. Solving these equations yields the solution for Poiseuille flow, as denoted by eq 3. To extend this concept to higher dimensions, we aim to construct "virtual tubing" in 2D and 3D geometries, which can be accomplished by utilizing a basic structure comprising two parallel plates, referred to as a flow layer throughout this article (Figure 1B). Although the velocity field within a flow layer differs from Poiseuille flow, it exhibits similarities, allowing further analysis and interpretation.

$$\frac{\partial^2 v_x}{\partial z^2} = \frac{1}{\mu}\frac{\partial p}{\partial x} \tag{4}$$

$$v_x\left(\frac{h}{2}\right) = 0 \tag{5}$$

$$v_x\left(-\frac{h}{2}\right) = 0 \tag{6}$$

$$v_x = \frac{h^2}{2\mu}\frac{\partial p}{\partial x}\left[\left(\frac{z}{h}\right)^2 - \frac{1}{4}\right] \tag{7}$$

where x and z are the components of the Cartesian coordinate system (Figure 1B), and h is the gap distance between the two parallel plates. The momentum equation is expressed as eq 4, accompanied by the no-slip boundary conditions given by eqs 5 and 6. The solution for the velocity field is provided in eq 7. A careful comparison between eqs 3 and 7 reveals a mere factor of 2 difference in the denominator, assuming identical pressure gradients. This discrepancy arises from the no-slip boundaries encountered in the capillary tubing and the flow layer plates. The no-slip boundary condition applies solely to a flow layer's top and bottom surfaces, resulting in reduced drag compared to the capillary tubing where fluids roundly perceive

https://doi.org/10.1021/acs.analchem.3c05982
Anal. Chem. 2024, 96, 5265−5273

drag along all sides of the tubing. By dividing eq 7 by 2, the velocity field transforms into a 2D Poiseuille flow. Therefore, we establish a virtual "2D tubing" using the flow layer configuration. Solving the Navier−Stokes equation within this flow layer and applying the division by 2, we can determine the position of the water/air interface, analogous to the principles underlying the Lucas−Washburn equation. We assume that the numerous overlaid parallel flow layers with heights h (flow layer set) obey a Gaussian distribution (Figure 1C)

$$g(\mathbf{h}) = \frac{1}{\sigma\sqrt{2\pi}}\exp - \frac{(h-\alpha)^2}{2\sigma^2} \tag{8}$$

where α is the mean gap height and σ is the standard deviation. Water/air interface locations are determined independently for each flow layer. The phase-field method is employed to differentiate between the two phases, where the water phase is denoted as $\phi = 1$ and the air phase as $\phi = 0$. At any given time and position, the distribution of the volumetric water content can be obtained by integrating the saturated flow layers and dividing by the total number of layers. This model is also applicable in three-dimensional space, necessitating the inclusion of a fourth dimension to accommodate the creation of flow layers. The general model equations are summarized below

$$\rho(\mathbf{u}\cdot\nabla)\mathbf{u} = -\nabla p + \mu\nabla^2\mathbf{u} \tag{9}$$

$$\frac{\partial\phi}{\partial t} = \frac{1}{\pi\left(\frac{h}{2}\right)^2}\int_0^{2\pi}\int_0^{h/2}\frac{\mathbf{u}(z)}{2}z\mathrm{d}z\mathrm{d}\varphi \tag{10}$$

$$\omega = \frac{\int_0^{+\infty}\pi(h/2)^2 g(h)\phi\mathrm{d}h}{\int_0^{+\infty}\pi(h/2)^2 g(h)\mathrm{d}h} \tag{11}$$

where ρ is the fluid density, eq 9 is the Navier−Stokes equation, eq 10 is the water/air interface migration velocity where the volumetric flow rate (the double integral) is divided by the cross-sectional area $\left(\pi\left(\frac{h}{2}\right)^2\right)$, and eq 11 is the water content distribution where the integral of saturated layers is divided by the total layers. The pore distribution is not limited to Gaussian function $g(h)$ and can be replaced by other distributions depending on the porous media. The upper and lower limits of eq 11, which represent the pore size range, can be set at certain values in practical applications (Supporting Information). Note that this is an equivalent model to calculate water content distribution, which means it does not use the exact microstructure or pore geometry of the porous media. The flow layer set is used to quantify the various flow velocities inside the porous media. Therefore, it can be used for different kinds of porous media like grain based and fiber based.

Experimental Setup. We used a nitrocellulose membrane (AE99, 13401787, Whatman) as the experimental porous media. To achieve the desired geometries, a laser cutter (VSL350, Universal Laser Systems) was used to cut the nitrocellulose sheets. For the one-dimensional problem, we employed nitrocellulose strips with dimensions of 5 mm width and 30 mm length. In the circular and droplet spreading problems, we utilized square nitrocellulose samples (7.5 × 7.5 cm). The strip dimensions for the fan-strip problem were set at a 2 mm width and 10 mm length. In the two-dimensional scenarios, we employed PEEK tubing (1569, IDEX) and a 1 mL syringe to ensure a continuous water supply by maintaining a small droplet (∼50 μL) around the point of contact between the tubing and the membrane, allowing the water to be absorbed and flow through the membranes. To avoid the water flowing above the membrane, the water supply from the tubing was maintained at a controlled rate (Figure 2A). Employing a small droplet as the water source allowed

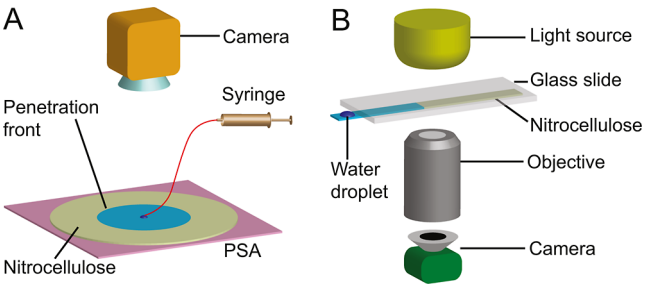

Figure 2. (A) Experimental setup to measure liquid penetration front. The small droplet is the water source supplied by a syringe and tubing. The video is taken by a camera. The figure shows the circular problem. (B) Experimental setup to measure water content by quantifying refractive index change on a microscope.

sufficient water absorption while preventing its overflow onto the membrane surface. This approach effectively balanced the need for providing excess water for absorption without inducing undesired flow above the membrane. In the droplet spreading experiment, a finite water source was employed instead of a continuous one. Specifically, a single 40 μL water droplet was carefully pipetted onto the nitrocellulose surfaces to serve as the water source. To obtain data on the relationship between penetration length L and time t, videos of the liquid flow process were captured and analyzed using ImageJ. To maintain data consistency, all experiments were implemented in the same conditions (temperature ∼23 °C and humidity ∼37−56%).[39]

Parameter Measurements. To obtain the contact angle, we fit one-dimensional experimental data measured on paper strips to the Lucas−Washburn equation[12]

$$L = \sqrt{\frac{\gamma h t\cos\theta}{4\mu}} \tag{12}$$

where L was the penetration length from the water source, γ was the water/air surface tension, θ was the contact angle, and μ was the dynamic viscosity. To simplify data processing, we utilized a squared form of the Lucas−Washburn equation, where the dependent variable was L^2, the independent variable was t, and the slope was denoted by $\frac{\gamma h\cos\theta}{4\mu}$. After the slope was obtained by linear regression of 1D experimental data, we determined the contact angle by plugging water/air surface tension γ, mean pore size r, and water dynamic viscosity μ into the slope and solving θ (see Supporting Information).[40]

The pore size was assumed to follow a Gaussian distribution. The mean pore size α was acquired from the manufacturer (Whatman). To obtain the standard deviation of the pore size, we utilized the change in water content within the partially saturated region. As the water content (ω) varied from 0 (unsaturated) to 1 (fully saturated), the refractive index of the membrane underwent corresponding changes according to the equation for light transmission (I) in a porous medium by Niemet and Selker[41]

https://doi.org/10.1021/acs.analchem.3c05982
Anal. Chem. 2024, 96, 5265−5273

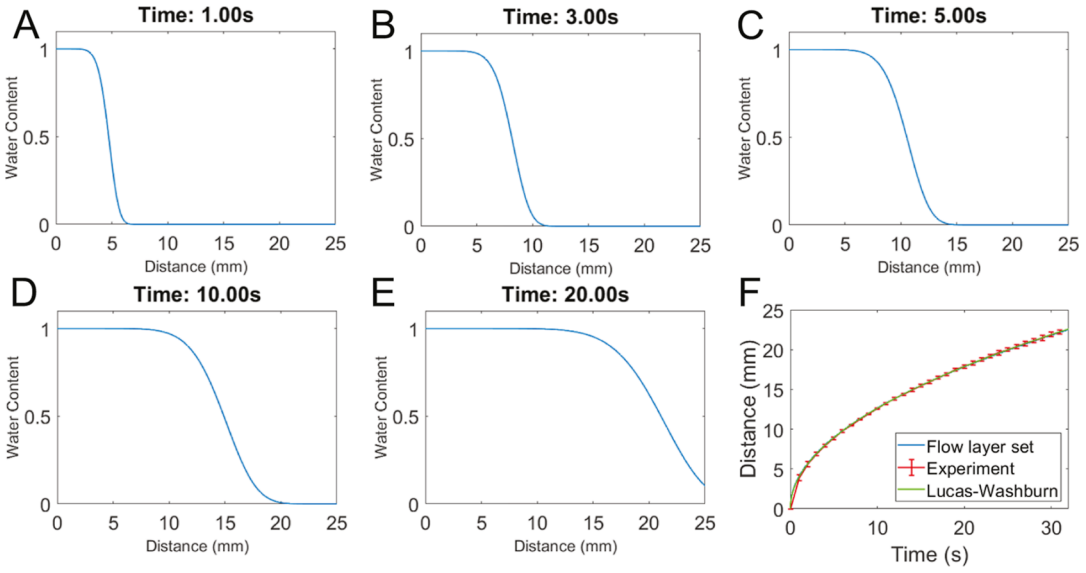

Figure 3. Water penetration depth over time in a 1D system. (A–E) Water penetration depth and water content at various simulation times. Both saturated and partially saturated regions migrate toward the dry region. (F) Comparison of penetration length L between the flow layer set model solution (blue), experimental data (red), and the Lucas–Washburn equation (green). Experiment error bars represent the standard deviation of 4 replicates.

$$\omega = 1 - \frac{\ln(I/I_s)}{\ln(I_d/I_s)} \tag{13}$$

where I was the light transmission intensity, I_d was the light transmission intensity of the porous medium in the dry state, and I_s was the light transmission intensity of the porous medium in the saturated state. We used microscopy (Axio Observer, Zeiss) to measure the intensity of light transmission through the nitrocellulose membrane and subsequently converted the data into water content values according to eq 13 (Figure 2B). By adjusting the standard deviation parameter in the model solution (eqs 9–11) until it matched the experimental results, we determined the value of the standard deviation, denoted as σ.

To determine the water content of the penetration front, we selected a specific water content value in the 1D solution of the flow layer set model and tracked its evolution throughout the entire simulation period, generating an L versus t curve. This curve was then compared with the corresponding experimental data. We iteratively adjusted the fixed water content value until it accurately matched the 1D experimental data. Then, this water content value was used for the penetration length.

Data Analysis. To assess the concordance between the values predicted by the model and those measured during the experiments, we employed root-mean-square error (RMSE) analysis using the following equation

$$\mathrm{RMSE} = \frac{\sqrt{\frac{1}{n}\sum_{i=1}^{n}(A_i - F_i)^2}}{\frac{1}{n}\sum_{i=1}^{n}A_i} \times 100 \tag{14}$$

where A_i was the actual value from the experiment and F_i was the forecast value from the model.

We visualized the model solutions in MATLAB (R2021a, MathWorks). The saturation was drawn according to the solved analytical solutions with the measured parameters. The predicted penetration length, L, was extracted from the saturation map according to the water content of the water front.

RESULTS

Parameters. The nitrocellulose membrane used in our study had a mean pore size of 8 μm, as provided by the manufacturer. By fitting the 1D data to the Lucas–Washburn eq (Supporting Information), we determined the contact angle to be 83.6°. Furthermore, we estimated the standard deviation of the pore size to be 4 μm by fitting the model to the water content data at four points with different distances (2.5, 5, 7.5, and 10 mm) from the water source (see Supporting Information). The water content of the penetration length was determined to be 82.5% by tracking and tuning the water content in the model until it matched the 1D experimental penetration length data.

One-Dimensional Problem. Paper strips find widespread utilization in lateral flow tests, akin to a simplified 1D representation of water flow within porous media.[30,31] Precisely determining the flow rate and water content within these strips has strong implications for the design and development of novel products. Examining the solution of the 1D problem, we predicted the migration of both the fully saturated and partially saturated regions (Figure 3A–E). The predicted penetration length (location of the water front at 82.5% saturation) as a function of time aligned closely with the experimental data (Figure 3F). To further compare the model predictions with the experimental data, we plotted the curve of the Lucas–Washburn equation using the measured parameters. As expected, the three curves closely coincided, providing evidence of the accuracy of our 1D solution. The RMSE between the model and experimental values was calculated to be 0.62%, affirming a strong agreement between them.

Circular Problem. Multiplexed detection of vital biomarkers with paper-based devices has been extensively discussed in the literature.[32,33] A comprehensive understanding of liquid flow dynamics is instrumental in the ongoing refinement and innovation of such devices. We developed a generalized circular spreading model to serve as a reference for the design and analysis of radial flow systems.[32,33] In the 2D circular flow experiment, water was supplied to the center of a

https://doi.org/10.1021/acs.analchem.3c05982
Anal. Chem. 2024, 96, 5265–5273

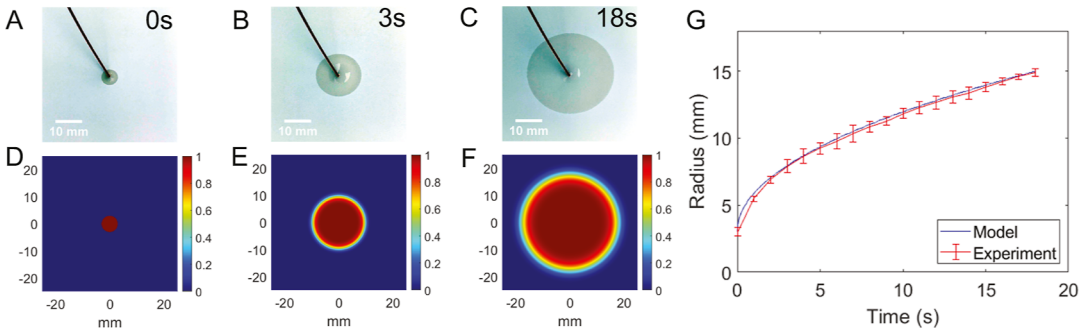

Figure 4. Experiment and model of 2D circular flow. (A–C) Photos of the circular experiment over time. The tubing provides a small circular water source. Water is absorbed and flows only through but not above the membrane in our observation. The photos are adjusted to increase the contrast for visualization. (D–F) Model predicted water content distribution. (G) Penetration length (radius) comparison of the model (blue) and experiment (red). Experiment error bars represent the standard deviation of 4 replicates.

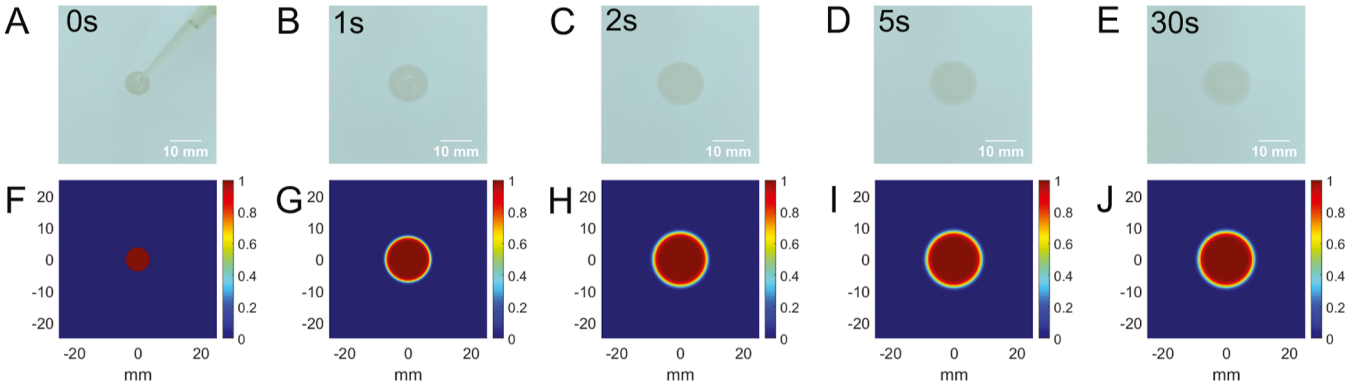

Figure 5. Experiment and model of 2D droplet spreading. (A–E) Experimental photos of droplet spreading on the 2D membrane over time. A 40 μL water droplet is released on nitrocellulose via a pipet. It extends radially and quickly stops. (F–J) Solution of our flow layer set model. After depleting the water, surface tension is balanced in all directions, containing the wetting region expansion.

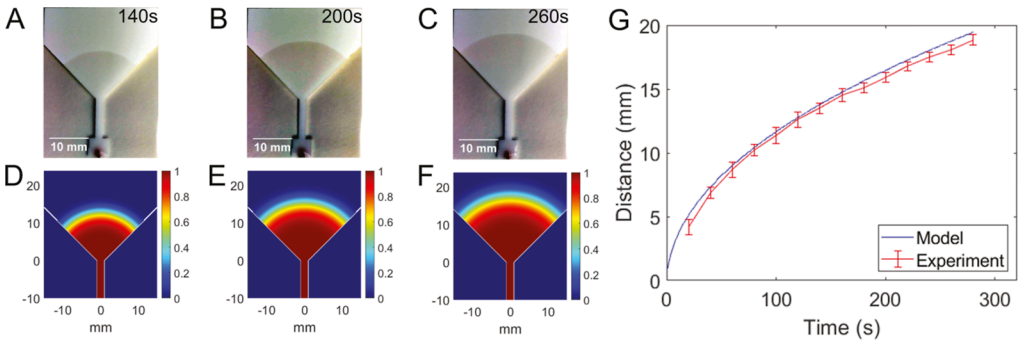

Figure 6. Experiment and model of 90° fan-strip spreading. (A–C) Photos of the fan experiment with central angle 90° imaged over time. The water penetration length is measured on the right edge of the fan. The photos are adjusted to increase the contrast. (D–F) Model solution images indicating the moisture distribution. The time of the images is the same as the experimental photos above. (G) Comparison between the model solution (blue) and experimental (red) fluid penetration length in the fan. Experiment error bars represent the standard deviation of 3 replicates. The experimental data are collected at the paper edge of the right side of the fan.

nitrocellulose membrane. The water was absorbed and migrated radially outward through the membrane (Figure 4A–C). Although this problem was 2D, we can simplify it by employing the cylindrical coordinate system to eliminate one variable, taking advantage of its inherent symmetry (Supporting Information). The saturated region remained circular around the source, while the partially saturated area formed an annulus (Figure 4D–F). The flow layer set model-predicted water front penetration length (location of 82.5% saturation) overlapped with the experimental data (Figure 4G). The calculated RMSE between the model and experiment was 1.40%, providing compelling evidence of a robust agreement between the penetration length solution and experimental data.

Limited Source Volume. If the total volume of the water source was limited in the circular problem, then the migration of the circular wetting region eventually halted upon complete water source depletion. The driving force for flow resided solely at the water–air interface, governed by surface tension-induced capillary pressure. The pressure gradient arose from the pressure drop between the capillary pressure at the water/air interface and the atmospheric pressure of the water source. Once the water was depleted, the surface tension was balanced

https://doi.org/10.1021/acs.analchem.3c05982
Anal. Chem. 2024, 96, 5265–5273

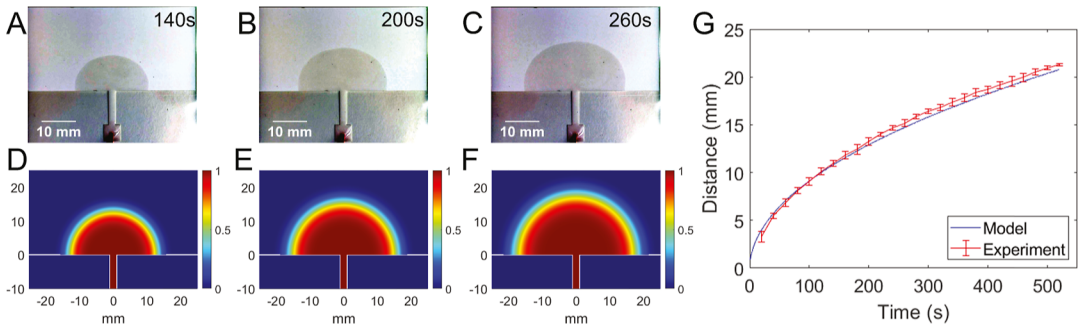

Figure 7. Experiment and model of 180° fan-strip spreading. (A–C) Photos of the fan experiment with central angle 180° imaged over time. We measured the penetration length on the right edge of the fan. The photos are adjusted to increase the contrast. (D–F) Model solution images indicating the moisture distribution. The time of the images is the same as the experimental photos above. (G) Comparison between the model solution (blue) and experimental (red) fluid penetration length in the fan. Experiment error bars represent the standard deviation of 4 replicates. The experimental data are collected at the paper edge of the right side of the fan.

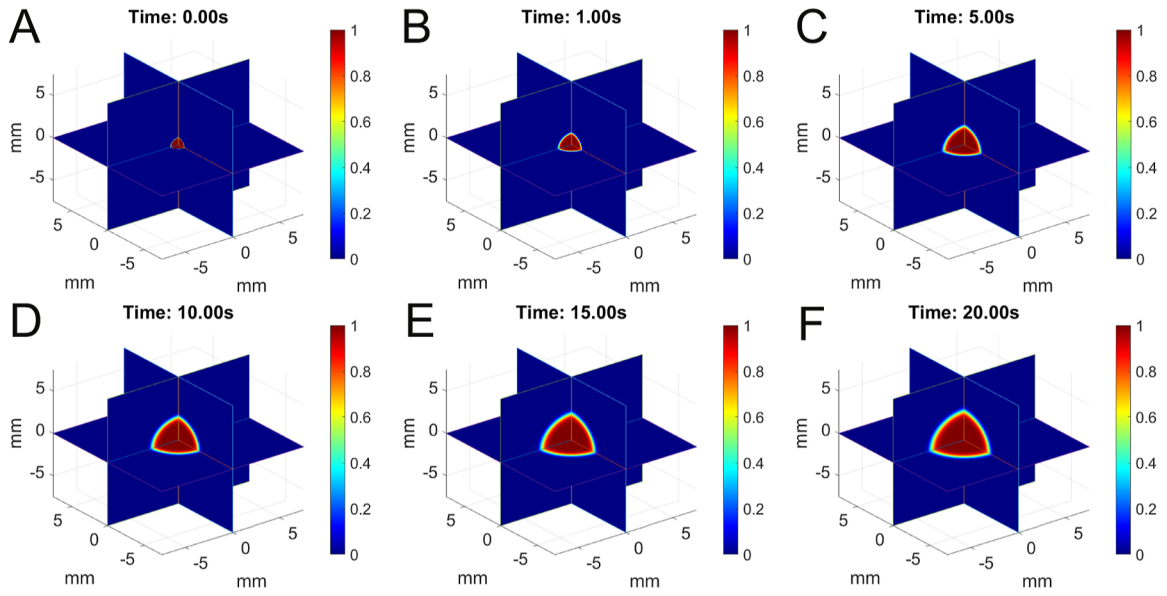

Figure 8. Model solution indicating moisture distribution in spherical problem over time (A–F). There is no experimental comparison due to lab resource limitations. The basic parameters used in this analytical solution are the same as those used for nitrocellulose in previous experiments.

in all directions and the pressure gradient became zero across the wetting area. Consequently, the expansion of the wetting region came to a standstill. We implemented an experiment using water droplets on a nitrocellulose membrane to validate this phenomenon (Figure 5A–E). Due to the hydrophilic nature of nitrocellulose, the water droplets were swiftly depleted, resulting in the cessation of wetting area expansion in approximately 2 s. Our model's solution accurately captured this behavior, as demonstrated by the agreement with experimental observations (Figure 5F–J). Notably, the analytical solution for this scenario was akin to the previous circular problem but with a limited water source. Once the water was depleted, the atmosphere pressure boundary condition in the center disappeared, leading to the balanced capillary pressure and the stopped-flow. Gonçalves et al. did a similar experiment with water droplets on fabric materials.[42] They got the same droplet phenomenon with our flow layer set model and experiments, which can be a comparison to our results.

Fan-Strip Problem. In the realm of paper-based microfluidics, the fan-strip configuration frequently serves as a flow pump for orchestrating fluid movement.[34−36] This application necessitates highly accurate flow rate data for effective control. The fan-strip geometry consisted of a paper strip and a fan (Figures 6 and 7). In the experimental setup, the junction between the fan and the strip served as a line source of water to the fan. For simplicity, we treated the junction as a point source, allowing us to approximate the fan as a sector of the circular problem with an angle of δ. On the other hand, the strip represented a 1D problem with a width denoted as w. Therefore, the analytical solution for the fan-strip configuration was valid only when the penetration length L in the fan region significantly exceeded the strip width, indicating $w/L \ll 1$ (see Supporting Information).

To ensure the validity of the solution, it was crucial to collect experimental data when L was sufficiently large compared to w, thereby ensuring that the system had reached a post-transient state. We examined two cases with central angles of 90 and 180° (Figures 6 and 7). The flow layer set model-predicted water front penetration length, which was the location of 82.5% saturation in the fan areas, overlapped with experimental data for both cases. The RMSE between the model and experiment was computed to be 3.69% for a central angle of 90° (Figure 6G) and 3.07% for a central angle of 180° (Figure

https://doi.org/10.1021/acs.analchem.3c05982
Anal. Chem. 2024, 96, 5265−5273

7G). These results confirmed a robust agreement between the flow layer set model and experimental outcomes.

Spherical Problem. In three-dimensional paper networks,[37,38] liquid flows along and through multiple layers of paper stacked together. While flow is controlled with hydrophobic or solid-phase barriers, knowing that the unbounded conditions can help to design efficient porous matrices. To demonstrate the model in 3D space, we solved a spherical problem involving a water source at the center from which water migrated radially in all directions in three-dimensional space. Given the symmetry of the sphere, an analytical solution can be obtained (see Supporting Information). To visually represent the solution, we incorporated the nitrocellulose parameters to depict the water content distribution (Figure 8), which indicated that saturated and partially saturated regions radially grew over time in all directions.

Permeability. Permeability, as used in Darcy's law, was typically determined through experimental measurements.[43,44] Our flow layer set model allowed for an analytical expression of permeability given the knowledge of pore size, standard deviation, and porosity. The volumetric flow rate Q in a porous medium was calculated by Darcy's law, denoted as Q_D, and our flow layer set model, denoted as Q_{fls}. The Q calculated by two different methods should be equal to $Q_D = Q_{fls}$ (see equation derivation in the Supporting Information), where Q_D contains permeability k. Solve for k and simplify the expression

$$k = \left\{\phi_p\left[\exp\left\{-\frac{\alpha^2}{2\sigma^2}\right\}\alpha\sigma(\alpha^2 + 5\sigma^2) + \sqrt{\frac{\pi}{2}}(\alpha^4 + 6\alpha^2\sigma^2 + 3\sigma^4)\left(1 + \mathrm{erf}\left(\frac{\alpha}{\sqrt{2}\sigma}\right)\right)\right]\right\} \Big/ \left\{2^5\left[\exp\left\{-\frac{\alpha^2}{2\sigma^2}\right\}\alpha\sigma + \sqrt{\frac{\pi}{2}}(\alpha^2 + \sigma^2)\left(1 + \mathrm{erf}\left(\frac{\alpha}{\sqrt{2}\sigma}\right)\right)\right]\right\} \quad (15)$$

where ϕ_p was the porosity, α and σ were the mean and the standard deviation of the pore size, and erf was the error function. Using this expression, the permeability can be calculated based on the provided parameters, eliminating the need for experimental measurements.

DISCUSSION

We found some researchers measured paper membranes' capillary pressure based on an inaccurate method,[21,45] which might mislead the analysis and design of paper devices. In their method, a saturated porous membrane strip was placed in a centrifuge, and the centrifugal force removed some of the water from the strip. They assumed that the remaining water resulted from the equilibrium between the centrifugal and capillary forces. However, this assumption may induce problems. The water−air interface is a closed Gaussian surface. If the water in porous media is not connected to an external water source, the capillary pressure in the porous media is balanced in all directions. Therefore, the presence of residual water in the membrane strip after centrifugation was due to the flow resistance and water−solid adhesion. Capillary pressure results from surface tension, surface energy, and pore size. The measured value by this method was larger than the actual capillary pressure.

Cummins et al. developed a porous media flow model based on the Washburn equation and Darcy's law.[46] The number of governing equations was equal to the number of pore sizes, which was hard to apply if the size range was large. Additionally, their model was restricted to 1D scenarios based on the Washburn equation. However, our flow layer set model was not restricted to these two aspects. The size range was continuous and determined by the upper and lower limits in the model eq (eq 11). The complexity did not increase as the pore size range grew. Furthermore, the flow layer set model was not limited to the 1D cases. We have demonstrated the feasibility of our model in 2D and 3D scenarios.

We excluded gravity from the flow layer set model and experiments for two reasons. First, all experimental procedures involved nitrocellulose membranes placed horizontally on the laboratory bench, rendering gravity inconsequential to the fluid flow direction. Furthermore, as assessed by Bond number,[47] a dimensionless parameter in fluid mechanics used to evaluate the relative influence of gravity and surface tension in fluid motion, it became evident that gravity's impact was minimal compared to surface tension. In our specific case, we calculated the Bond number to be 8.7×10^{-7}, signifying a significantly small value that justified the omission of gravity.

In the circular problem with the water supply at the center (Figure 4), we observed that the penetration front moved slower than that of the 1D problem. This discrepancy arose due to the differing geometries of the two scenarios. Specifically, as the radius r increased in the circular case, the surface area of the circle S followed a squared growth pattern described by $S = \pi r^2$. Consequently, for an arbitrary increment dr in the radius, the corresponding increase in the surface area became $dS = 2\pi r\, dr$, resulting in a larger wetted membrane area for the same dr as r increases. However, the relationship between the surface area and distance (radius) remained linear for a one-dimensional paper strip, leading to a faster growth rate than the 2D circular case. Similarly, the 3D spherical problem's penetration front advanced even slower than the two-dimensional case. This was attributed to the additional dimension, where the volume increased as $dV = 4\pi r^2\, dr$ in a sphere. Consequently, more time was required to pump the water and achieve saturation within the spherical shell domain. As a result, the penetration front of the 3D spherical problem exhibited the slowest migration rate among all of the cases investigated in this study. Hence, it should be noted that liquid flow within a 3D paper network was expected to necessitate a longer time and a larger volume of liquid compared to those of 1D and 2D systems, a factor that warranted careful consideration by researchers.

In the context of the limited source volume problem, when the pore size range is considerably broad, water may continue to spread, even after the water source has been exhausted. This phenomenon arises from the fact that smaller pores possess lower capillary pressure compared with larger pores. Consequently, water within the larger pores can function as micro water sources, enabling the extraction of water by smaller pores, a scenario aptly described by the Richards equation. However, in porous media with a narrow pore size range, as exemplified by the nitrocellulose material employed in this study, the differences in capillary pressures between large and small pores are insufficient to facilitate water flow. Thus, upon depletion of the water source, the surface tension acts radially to establish equilibrium, ultimately halting the spread of water.

In the 180° case of the fan-strip problem (Figure 7), we observed a slight elongation of the wetting area in the horizontal direction within the fan region (Figure 7A−C),

https://doi.org/10.1021/acs.analchem.3c05982
Anal. Chem. 2024, 96, 5265−5273

whereas the model predicted a semicircular shape (Figure 7D−F). This shape disparity arose from the simplification of the line source in the model, which assumed a circular solution resulting in a half-circle shape. When the condition $w/L \ll 1$ was satisfied, the experimental wetting area within the fan could be approximated as a half-circle. In the experiment, the penetration propagated synchronously in all directions while the line source expanded the wetting area predominantly horizontally. A similar trend was observed in the case of the fan-strip problem with the central angle of 90°. The wetting area near the two edges exhibited a slightly extended movement, resulting in an imperfect quadrant (Figure 6D−F). This behavior can also be attributed to the line source of the water.

Notably, we utilized a CCD camera and an inverted microscope to measure the refractive index change, to calculate the water content. We did not use a refractometer because the microscope can focus on a smaller measurement point (46 μm in diameter) than a refractometer (usually 1 mm to 1 cm in diameter). Therefore, the microscope can give better accuracy of the refractive change measurement.

In our analysis, we employed the assumption of an infinite pore size range, which was consistently applied throughout this study. Nevertheless, it is worth noting that pores exceeding a certain threshold value became inconsequential, as most porous media in experimental settings do not exhibit exceedingly large pores. Therefore, it is advisable to define specific upper and lower limits based on empirical measurement data, thereby refining the pore size range to better align with the characteristics of the porous medium under investigation. Such refinement not only enhances the accuracy of the analysis but also reduces the computational intensity, particularly in numerical simulations.

We highlight several key points in our study. First, it is notable that we assumed that the pores within the porous media are randomly distributed to maintain properties such as the porosity and permeability isotropic throughout the entire domain of interest through this study. Nonisotropic media can also be modeled but only with knowledge of the spatial distribution of pore size. Second, our analytical solutions consider only capillary pressure without other pressures, and the influence of gravity was negligible. Our model is based on the Navier−Stokes equation, allowing for the inclusion of additional pressures in the pressure gradient term ∇p. Third, our solutions only included two-phase flows, focusing on the capillary pressure at the water/air/solid interface. During the solution of the analytical solutions, we exclusively calculate the water phase while disregarding the airflow due to the significantly low air pressure. In cases where a membrane is enclosed on both sides, the air pressure becomes a crucial factor, necessitating the solution of the Navier−Stokes equation in both phases. Moreover, our model can be extended to handle systems with more phases, such as three immiscible phases, where capillary pressures exist at all fluid/fluid/solid interfaces, such as oil/water/air interfaces.

We also implemented experiments (1D, circular, fan-strip with central angles of 90 and 180°) on cellulose membranes. The measured cellulose parameters were plugged into the solution to obtain model results. The measured experimental data agreed closely with the model (see Supporting Information). This model exhibited consistent performance on both nitrocellulose and cellulose substrates.

CONCLUSIONS

We developed a novel two-phase porous media flow model, named the flow layer set model, based on the Navier−Stokes equation. We expanded the tubing concept to higher dimensions and created 2D and 3D "virtual tubing" by the configuration of a flow layer. The flow layer heights were assumed to obey the Gaussian distribution. The water content in the porous media can be calculated by integrating the saturated flow layers. The key parameters of this model were the pore size distribution and the contact angle. We identified five analytical solutions (one-dimensional problem, circular problem, fan-strip problem, spherical problem, and permeability of Darcy's law). Experimental data agreed closely with the model solutions for both nitrocellulose and cellulose, confirming the validity and accuracy. Our model can be readily employed in other research areas where a two-phase porous media flow is of significant interest.

ASSOCIATED CONTENT

Supporting Information

The Supporting Information is available free of charge at https://pubs.acs.org/doi/10.1021/acs.analchem.3c05982.

The details of the equation derivation, including the analytical solution expressions, are in the Supporting Information (PDF)

AUTHOR INFORMATION

Corresponding Authors

Tamara L. Kinzer-Ursem − *Weldon School of Biomedical Engineering, Purdue University, West Lafayette, Indiana 47907, United States;* orcid.org/0000-0001-7343-115X; Email: tursem@purdue.edu

Jacqueline C. Linnes − *Weldon School of Biomedical Engineering, Purdue University, West Lafayette, Indiana 47907, United States;* orcid.org/0000-0003-4962-0908; Email: jlinnes@purdue.edu

Author

Hui Ma − *Weldon School of Biomedical Engineering, Purdue University, West Lafayette, Indiana 47907, United States;* orcid.org/0000-0003-2321-3781

Complete contact information is available at: https://pubs.acs.org/10.1021/acs.analchem.3c05982

Notes

The authors declare no competing financial interest.

ACKNOWLEDGMENTS

The authors thank Prof. Arezoo M. Ardekani, Dr. Miad Boodaghidizaji, and lab members in J.C.L. lab and T.K.U lab for helpful discussions, especially Lucy T. Tecle, Barrett F. Davis, and Luke P. Brennan for reviewing the manuscript. This work was supported in part by the National Science Foundation (NSF) award 1752366, National Institutes of Health (NIH) National Institute on Drug Abuse DP2 DA051910, NIH National Cancer Institute R01 CA246315, and Gordon and Betty More Foundation (GBMF) Moore Inventor Fellowship Grant 9687. The content is solely the responsibility of the authors and does not necessarily represent the official views of the NSF, NIH, or GBMF.

REFERENCES

(1) Singh, K.; Jung, M.; Brinkmann, M.; Seemann, R. *Annu. Rev. Fluid. Mech.* **2019**, *51*, 429−449.
(2) Xiong, Y. *J. Hydrol.* **2014**, *510*, 353−362.
(3) Cai, J.; Hu, X.; Standnes, D. C.; You, L. *Colloids Surf., A* **2012**, *414*, 228−233.
(4) Adler, P. M.; Thovert, J.-F. *Appl. Mech. Rev.* **1998**, *51*, 537−585.
(5) Darcy, H. *Les fontaines publiques de la ville de Dijon: exposition et application*; Victor Dalmont, 1856.
(6) Whitaker, S. *Transp. Porous Media* **1986**, *1*, 3−25.
(7) Rodríguez de Castro, A. *Adv. Water Resour.* **2019**, *126*, 55−64.
(8) Bauer, D.; Talon, L.; Peysson, Y.; Ly, H. B.; Batot, G.; Chevalier, T.; Fleury, M. *Phys. Rev. Fluids* **2019**, *4*, 063301.
(9) Brinkman, H. C. *Flow, Turbul. Combust.* **1949**, *1*, 27−34.
(10) Durlofsky, L.; Brady, J. *Phys. Fluids* **1987**, *30*, 3329−3341.
(11) Dukhan, N. *J. Fluid Eng.* **2012**, *134*, 071201.
(12) Washburn, E. W. *Phys. Rev.* **1921**, *17*, 273−283.
(13) Hamraoui, A.; Nylander, T. *J. Colloid Interface Sci.* **2002**, *250*, 415−421.
(14) Fisher, L. R.; Lark, P. D. *J. Colloid Interface Sci.* **1979**, *69*, 486−492.
(15) Cai, J.; Jin, T.; Kou, J.; Zou, S.; Xiao, J.; Meng, Q. *Langmuir* **2021**, *37*, 1623−1636.
(16) Richards, L. A. *Physics* **1931**, *1*, 318−333.
(17) Farthing, M. W.; Ogden, F. L. *Soil Sci. Soc. Am. J.* **2017**, *81*, 1257−1269.
(18) Barry, D.; Parlange, J.-Y.; Sander, G.; Sivaplan, M. *J. Hydrol.* **1993**, *142*, 29−46.
(19) Pachepsky, Y.; Timlin, D.; Rawls, W. *J. Hydrol.* **2003**, *272*, 3−13.
(20) Perez-Cruz, A.; Stiharu, I.; Dominguez-Gonzalez, A. *Microfluid. Nanofluidics* **2017**, *21*, 98.
(21) Rath, D.; Sathishkumar, N.; Toley, B. J. *Langmuir* **2018**, *34*, 8758−8766.
(22) Gasperino, D.; Baughman, T.; Hsieh, H. V.; Bell, D.; Weigl, B. H. *Annu. Rev. Anal. Chem.* **2018**, *11*, 219−244.
(23) Dullien, F. *Mathematical Modeling for Flow and Transport through Porous Media*; Springer, 1991; pp 581−606.
(24) Manlowe, D. J.; Radke, C. J. *SPE Reservoir Eng.* **1990**, *5*, 495−502.
(25) Nabovati, A.; Sousa, A. *New Trends in Fluid Mechanics Research*; Springer, 2007; pp 518−521.
(26) Ovaysi, S.; Piri, M. *J. Comput. Phys.* **2010**, *229*, 7456−7476.
(27) Joekar-Niasar, V.; Hassanizadeh, S. *Crit. Rev. Environ. Sci. Technol.* **2012**, *42*, 1895−1976.
(28) Raoof, A.; Hassanizadeh, S. M. *Transp. Porous Media* **2010**, *81*, 391−407.
(29) Suchomel, B. J.; Chen, B. M.; Allen III, M. B. *Transp. Porous Media* **1998**, *30*, 1−23.
(30) Sritong, N.; Sala de Medeiros, M.; Basing, L. A.; Linnes, J. C. *Lab Chip* **2023**, *23*, 888−912.
(31) Carrell, C.; Kava, A.; Nguyen, M.; Menger, R.; Munshi, Z.; Call, Z.; Nussbaum, M.; Henry, C. *Microelectron. Eng.* **2019**, *206*, 45−54.
(32) Noviana, E.; Ozer, T.; Carrell, C. S.; Link, J. S.; McMahon, C.; Jang, I.; Henry, C. S. *Chem. Rev.* **2021**, *121*, 11835−11885.
(33) Karita, S.; Kaneta, T. *Anal. Chem.* **2014**, *86*, 12108−12114.
(34) Tokihiro, J. C.; Tu, W.-c.; Berthier, J.; Lee, J. J.; Dostie, A. M.; Khor, J. W.; Eakman, M.; Theberge, A. B.; Berthier, E. *Phys. Fluids* **2023**, *35*, 082120.
(35) Shay, T.; Saha, T.; Dickey, M. D.; Velev, O. D. *Biomicrofluidics* **2020**, *14*, 034112.
(36) Wang, X.; Hagen, J. A.; Papautsky, I. *Biomicrofluidics* **2013**, *7*, 014107.
(37) Martinez, A. W.; Phillips, S. T.; Whitesides, G. M. *Proc. Natl. Acad. Sci. U.S.A.* **2008**, *105*, 19606−19611.
(38) Li, X.; Ballerini, D. R.; Shen, W. *Biomicrofluidics* **2012**, *6*, 11301.
(39) Hoilett, O. S. WEARABLES SENSORS FOR MONITORING SUBSTANCE USE DISORDER PATIENTS. Ph.D. Thesis, Purdue University Graduate School, 2021.
(40) Nguyen, N.-T.; Wereley, S. T.; Shaegh, S. A. M. *Fundamentals and Applications of Microfluidics*; Artech House, 2019.
(41) Niemet, M. R.; Selker, J. S. *Adv. Water Resour.* **2001**, *24*, 651−666.
(42) Gonçalves, M.; Kim, J. Y.; Kim, Y.; Rubab, N.; Jung, N.; Asai, T.; Hong, S.; Weon, B. M. *Sci. Rep.* **2022**, *12*, 1087.
(43) Scherer, G. W. *J. Non-Cryst. Solids* **1989**, *113*, 107−118.
(44) Honarpour, M.; Mahmood, S. *J. Petrol. Technol.* **1988**, *40*, 963−966.
(45) Buser, J. R. Heat, Fluid, and Sample Control in Point-of-Care Diagnostics. Ph.D. Thesis, University of Washington, 2016.
(46) Cummins, B. M.; Chinthapatla, R.; Ligler, F. S.; Walker, G. M. *Anal. Chem.* **2017**, *89*, 4377−4381.
(47) Panton, R. L. *Incompressible Flow*; John Wiley & Sons, 2013.

https://doi.org/10.1021/acs.analchem.3c05982
Anal. Chem. 2024, 96, 5265−5273